# Nd-Co substituted strontium hexaferrite powders with enhanced coercivity

C. A. Herme[a], P. G. Bercoff[b*] and S. E. Jacobo[a]

[a] *Facultad de Ingeniería, Universidad de Buenos Aires, LAFMACEL-INTECIN. Paseo Colón 850, 1063 Buenos Aires, Argentina*

[b] *Facultad de Matemática, Astronomía y Física, Universidad Nacional de Córdoba. IFEG, CONICET. Ciudad Universitaria. 5000 Córdoba, Argentina*

**Corresponding author.* e-mail: bercoff@famaf.unc.edu.ar.
Tel: (+54) 351 433 4051. Fax: (+54) 351 433 4054

---

Abstract

In this work we report the synthesis of Nd-Co substituted strontium hexaferrites of composition $Sr_{1-x}Nd_xFe_{11-x}Co_xO_{19}$ by the sol-gel auto-combustion method with further heat treatment. The analysis of the X-ray diffraction spectra shows the M-type hexagonal structure in samples treated at 1100ºC for two hours. Coercivity increases 11 % with 0.2 Nd-Co substitution, reaching a value of 68.9 A/m (5480 Oe) while saturation magnetization is reduced 6% to 91 $Am^2/kg$ (91 emu/g). The behavior of magnetic susceptibility with an applied field shows two different maxima which are assigned to different magnetic orderings. This assumption is supported by the appearence of two experimental values of Curie temperatures ($T_C$) for all the prepared samples. Magnetic susceptibility $\chi$ and $T_C$ measurements suggest an uneven distribution of the iron vacancies.

KEYWORDS: A. magnetic materials, B. sol-gel chemistry, C. X-ray diffraction, D. magnetic properties, D. magnetic structure.

## 1. Introduction

Hexagonal ferrites have been widely used as permanent magnets since their discovery in the 1950s. In spite of their relatively modest magnetic properties, the ferrite magnets still show the best performance to cost ratio [1]. However, efforts are being made to improve their magnetic capabilities by using different synthesis methods [2-4].

New processes have been attempted to prepare nano-sized single-domain particles [5,6]. In most cases the**se** attempt**s** to get single-phase materials failed when the heat-treatment temperature remained below 1200ºC, producing large multi-domain particles not suitable for recording applications.

J. F. Wang *et al.* have investigated Sm-doped Sr hexaferrite particles hydrotermally synthesized [7]. They found that, unlike transition metal element substitution, samarium substitution does not decrease the hexaferrite particle size. The intrinsic coercivities of Sm-doped Sr hexaferrite are significantly higher than those of non-substituted strontium hexaferrite. By the same chemical process, Wang *et al.* prepared Nd-substituted Sr hexaferrite [8]. The samples needed to be calcined above 1150ºC in order to avoid secondary phases. They reported that for Nd-Sr ratio of 1/8, the saturation magnetization $M_S$ value is almost the same as that of non-substituted Sr ferrite, whereas its coercivity (325 kA/m or 4300 Oe) is a value approximately 11% higher than that of the non-substituted sample. In both reports secondary phases such as $SrFeO_3$ and $NdFeO_3$ were observed for all the R-Sr (R = rare earth ions) substitutions.

H. Taguchi *et al.* [9] and F. Kools *et al.* [10] have reported that the saturation magnetization as well as the magnetocrystalline anisotropy constant of magnetoplumbite ferrite fine particles were increased by the substitution of La and Co ions. Different scientific investigations and techniques

(Mössbauer spectrometry, X-ray diffraction, magnetic measurements) have optimized the permanent magnet properties of La-Co substituted hard ferrite magnets with the $Sr_{1-x}La_xFe_{12-y}Co_yO_{19}$ composition. For $y=x$, the magnetic properties increase up to $x=0.2$, and then decrease due to the presence of secondary phases containing La and Co, and to lateral grain growth during sintering [11]. It has also been observed that La excess induces the decoupling of the particles, thus enhancing the coercivity [12]. However, the solubility of rare earth ions in strontium M-type hexaferrite is very low and their introduction leads to the formation of secondary phases, which must be avoided in order to obtain permanent magnets with optimal properties.

More recently, L. Lechevallier *et al.* [13] reported the results of the structural investigation of $Sr_{1-x}R_xFe_{12}O_{19}$ and $Sr_{1-x}R_xFe_{12-x}Co_xO_{19}$ (R=Pr, Nd) hexaferrite powders prepared by the conventional ceramic process**.** They discussed the influence of the presence of Co on the rare earth ions solubility in the M-type phase. X-ray diffraction analysis of the calcined materials showed the presence of secondary phases in substituted samples. However, for the same x value, the proportion of secondary phases is lower in Co-containing powders than in the Co-free ones.

The citrate self-combustion process has also been tried for La-Co substituted hexagonal ferrite [14] where a complete single-phase formation was only observed for annealing temperatures above 1200ºC.

Previous work in our laboratory [15] has shown that single-phase hexaferrites can be obtained after annealing at 1100 ºC for 2h. When a strong iron deficiency with substitution is formulated ($Sr_{1-x}Nd_xFe_{12(1-x)}Co_xO_{19}$), coercivity increases from 26.40 A/m (2100 Oe) for $x=0$ to 58.70 A/m (4670 Oe) for $x=0.3$. However, a large iron deficiency gives rise to an important disturbance in site occupancy, especially at the 12k site [16]. In order to extend these investigations, and since the mentioned effect was not observed for the stoichiometric Fe/Sr ratio (=12) nor for the ratio Fe/Sr=11, samples of composition $Sr_{1-x}Nd_xFe_{11-x}Co_xO_{19}$ were prepared by the sol-gel autocombustion method and subsequent annealing at 1100ºC for 2h and for 12h. The magnetic behavior of these materials is compared to previously reported results [15,16].

## 2. Experimental

Samples of composition $Sr_{1-x}Nd_xFe_{11-x}Co_xO_{19}$ ($x$=0.00; 0.10; 0.20; 0.30; 0.40 and 0.50) were prepared by the self-combustion method. The chemical precursors used for these experiments were $SrCO_3$, $Nd_2O_3$, $Fe(NO_3)_3 \cdot 9H_2O$, $Co(CH_3COO)_2 \cdot 4H_2O$. The precursors were weighed according to different $Sr^{2+}$-$Nd^{3+}$-$Fe^{3+}$-$Co^{2+}$ mole ratios and completely dissolved in small amounts of a nitric acid solution. Then the pH was adjusted to ~7 by adding ammonium hydroxide. When citric acid, $C(COOH)OH(CH_2COOH)_2$, was added, the result was a sol of metal hydroxides and ammonium nitrate. The ratio citric:nitric acid was fixed in 2:1 for each experiment and the pH was fixed at about 7 with ammonium hydroxide.

The aqueous suspensions were stirred and heated for several hours until the sol turned into a dried gel. Then the dried gel ignited in a corner and a combustion wave was spontaneously propagated through the whole gel converting it into a loose magnetic powder. After a quick combustion, the powders were heated at 400ºC for one hour to eliminate the residual organic compounds. Then the powders were heat-treated in an air atmosphere at 1100ºC for two or twelve hours. In this way, two sets of samples were obtained: My-2 and My-12, where "y" stands for the Nd-Co composition. The compositions and labels for the samples with different thermal treatments are shown in Table 1.

The structural analysis of the powders was done by X-ray diffraction using a Philips diffractometer and CuKα radiation. The patterns were taken between $2\theta$=20º and 70º with a step size of 0.02º and acquisition time of 5 seconds per step. Lattice parameters and mean size were determined for each sample by means of the Rietveld method with the aid of the software TOPAS®. The refinements were made on patterns taken under special conditions: a range in $2\theta$ from 15º to 90º and 9 seconds of counting time per step.

Table 1. Labels for samples of different composition and with different thermal treatments. Cationic composition as determined by ICP is also shown.

| Heat treatment / Nominal composition | Powder calcination $t$=2 h $T$=1100ºC | Powder calcination $t$=12 h $T$=1100ºC | Experimental cationic composition (ICP) |
|---|---|---|---|
| $SrFe_{11}O_{19}$ | M0-2 | M0-12 | $SrFe_{10.9}$ |
| $Sr_{0.9}Nd_{0.1}Fe_{10.9}Co_{0.1}O_{19}$ | M10-2 | M10-12 | $Sr_{0.90}Nd_{0.11}Fe_{10.8}Co_{0.10}$ |
| $Sr_{0.8}Nd_{0.2}Fe_{10.8}Co_{0.2}O_{19}$ | M20-2 | M20-12 | $Sr_{0.77}Nd_{0.21}Fe_{10.5}Co_{0.17}$ |
| $Sr_{0.7}Nd_{0.3}Fe_{10.7}Co_{0.3}O_{19}$ | M30-2 | M30-12 | $Sr_{0.68}Nd_{0.32}Fe_{10.4}Co_{0.31}$ |
| $Sr_{0.6}Nd_{0.4}Fe_{10.6}Co_{0.4}O_{19}$ | M40-2 | M40-12 | $Sr_{0.57}Nd_{0.42}Fe_{10.2}Co_{0.41}$ |
| $Sr_{0.5}Nd_{0.5}Fe_{10.5}Co_{0.5}O_{19}$ | M50-2 | M50-12 | $Sr_{0.44}Nd_{0.48}Fe_{9.4}Co_{0.49}$ |

Inductively coupled plasma atomic emission spectrometry (ICP AES) with an ultrasonic nebulization system was performed with Baird ICP 2070 equipment. Measurements were carried out using a calibration curve obtained from standards of known concentration in 10% (v/v) HF medium. The analytical conditions were optimized in order to achieve the appropriate sensitivity. Samples were digested with a 1 : 1 nitric acid–perchloric mixture. The analytical detection limit was 0.4 ug/L.

A vibrating sample magnetometer Lakeshore 7300 was used to measure magnetic properties at room temperature. Hysteresis loops *M vs H* were measured with a maximum applied field of 15 kOe (190 A/m). Since the loops did not saturate at 15 kOe, the saturation magnetization $M_S$ for each sample was calculated by extrapolating to 0 *M vs* 1/*H*.

Scanning Electron Microscopy (SEM) images were taken with a microscope Zeiss DSM 982 GEMINI.

The Curie temperature $T_C$ was determined using a differential calorimeter SDT Q600 (TA Instruments) in $N_2$ atmosphere and under magnetic field. The heating rate was 10ºC/min. TG curves of weight *vs* temperature were used to determine $T_C$ using the tangent method.

## 3. Results and Discussion

X-ray analysis reveals that, in the patterns of all samples calcined for 2 h, the main peaks correspond to the hexagonal M-type phase while some secondary phases are found for $x \geq 0.2$ (Fig. 1). The results obtained for the samples calcined for 12 h are very similar to the ones in Fig. 1 and are not shown.

Rietveld refinements were performed for all the samples with the software TOPAS®. The model structure used for refining the hexaferrite is ICSD 202518 and for the secondary phases ICSD 66756 (hematite), ICSD 98553 ($CoFe_2O_4$) and ICSD 153441 ($NdFeO_3$). Neither occupancy factors nor thermal parameters were refined.

Figure 2 a and b show the corresponding refinements for samples with $x$=0.3 calcined for 2 and 12 h, respectively, and Table 2 contains the Rietveld refinement factors $R_{exp}$, $R_{wp}$, $R_{Bragg}$ (for the hexaferrite) and the Goodness of Fit (GOF). It is remarkable that the GOF is around 1 in every case.

In the set My-2, the mean crystallite size $D$, as given by Rietveld refinements decreases with $x$, as shown in Table 2. Samples M0-2 and M10-2 are single-phase, while for $x \geq 0.2$ small amounts of hematite $\alpha$-$Fe_2O_3$ appear, increasing with $x$. Secondary phases of Nd and Co ($NdFeO_3$ and $Co_2FeO_4$) are formed for substitutions of $x \geq 0.3$ (Table 2).

In the set My-12, the mean crystallite size also decreases with $x$, but in every case the value is larger than the value obtained for the corresponding composition calcined for 2 h. This is consistent with grain-growth due to longer calcination time. Some hematite is segregated in the samples with longer time of heat-treatment, but the fraction is lower than the amount observed for 2 h.

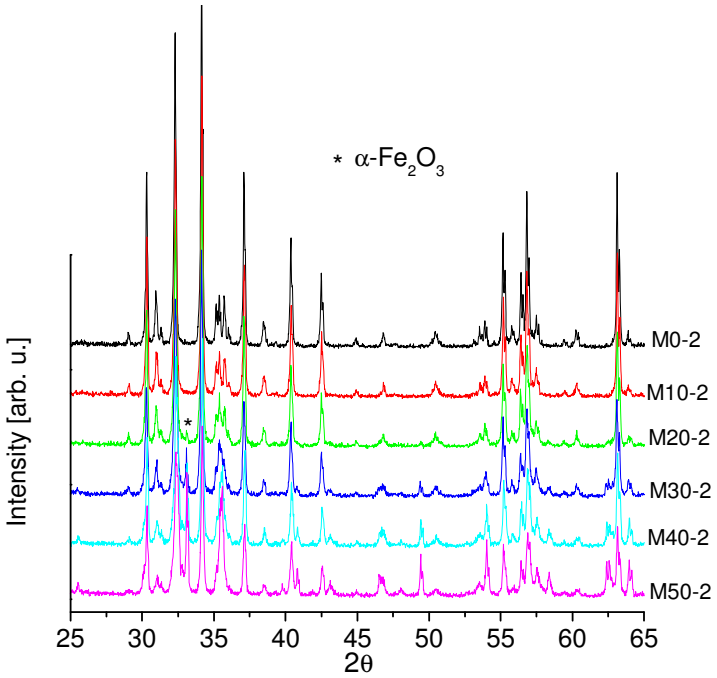


Fig. 1. XRD spectra of samples calcined for 2 hours. All major reflections correspond to the hexagonal phase M. Some secondary phases are noticed for $x \geq 0.2$ but only the most intense peak of hematite is indexed here for the sake of clarity, leaving all the others unindexed (Table 2).

In particular, sample M30-12 is single-phase, in contrast with sample M30-2 which has also hematite, Nd ferrate and $Co_2FeO_4$ (see Fig. 2). In samples My-12, the same Nd and Co secondary phases are observed, starting from $x$=0.4. This indicates that longer calcination times promote Nd and Co inclusion in the hexagonal lattice therefore, avoiding secondary phases for $x$ values below 0.4. It is also observed that the amounts of Nd ferrate and $Co_2FeO_4$ that appear for $x \geq 0.4$ are smaller in the samples calcined for 12 h than the corresponding ones in the set calcined for 2 h.

SEM images of the samples calcined for 2 h are shown in Fig. 3a to 3f (M0-2 to M50-2, respectively). Regardless of the Nd content, all the particles are hexagonal platelets of the order of 100 nm; size and shape are not noticeably modified with the substitution. However, this is not the case for the samples calcined for 12 h, as shown in Fig. 4a to 4f (M0-12 to M50-12, respectively). The particles in samples M0-12 and M10-12 approximately double their mean size with respect to the same samples calcined for 2 h (see Fig. 4a and 4b). The rest of the samples show a small decrease in particle size and evidence a slight sintering among the grains (see Fig. 4c to 4f). When secondary phases are segregated, both crystal and grain size (refer to Table 2 and Fig. 4c to 4f, respectively) are not substantially modified by a longer heat-treatment. This effect of grain-growth inhibition because of the appearance of secondary phases has already been reported by other authors [17]. In all samples, a unimodal distribution of particles size ($d$ ) was measured. Figure 5 shows histograms for the particle size distribution of samples M0-2 to M50-2, where a single distribution can be noticed for each one. Note that $d$ is larger than the crystal size $D$ given in Table 2. This effect is not surprising as the crystallite size $D$ is related to the crystalline planes orientation while the particle size $d$ refers to a single grain.

Table 2. Lattice parameters, mean crystal size *D* and % of segregated phases in samples calcined for 2 and 12 hours. Rietveld refinement factors are also shown.

| Sample | *a* [±0.0001Å] | *c* [±0.0008Å] | $V_{cell}$ [±1Å$^3$] | *D* [±1nm] | % segr. $Fe_2O_3$ [±0.2%] | % segr. $NdFeO_3$ [±0.2%] | % segr. $Co_2FeO_4$ [±0.2%] | $R_{exp}$ | $R_{wp}$ | $R_{Bragg}$ (hexaferrite) | GOF |
|---|---|---|---|---|---|---|---|---|---|---|---|
| M0-2 | 5.8798 | 23.0321 | 689 | 122 | - | - | - | 9.02 | 14.34 | 4.17 | 1.59 |
| M10-2 | 5.8781 | 23.0176 | 689 | 100 | - | - | - | 10.03 | 13.31 | 2.89 | 1.33 |
| M20-2 | 5.8790 | 23.0102 | 689 | 88 | 2.6 | - | - | 9.71 | 14.42 | 3.47 | 1.48 |
| M30-2 | 5.8767 | 23.0040 | 688 | 87 | 7.4 | 3.9 | 5.0 | 9.62 | 11.78 | 2.24 | 1.22 |
| M40-2 | 5.8739 | 22.9826 | 687 | 85 | 13.3 | 5.8 | 8.6 | 9.26 | 13.41 | 3.39 | 1.45 |
| M50-2 | 5.8773 | 22.9985 | 688 | 78 | 21.6 | 8.3 | 11.6 | 8.67 | 11.6 | 2.5 | 1.28 |
| | | | | | | | | | | | |
| M0-12 | 5.8797 | 23.0346 | 689 | 132 | - | - | - | 10.48 | 15.85 | 3.99 | 1.51 |
| M10-12 | 5.8778 | 23.0170 | 689 | 112 | - | - | - | 10.55 | 15.67 | 4.25 | 1.48 |
| M20-12 | 5.8779 | 23.0066 | 688 | 89 | - | - | - | 10.17 | 14.14 | 3.42 | 1.42 |
| M30-12 | 5.8756 | 22.9956 | 688 | 86 | - | - | - | 10.16 | 15.16 | 3.51 | 1.49 |
| M40-12 | 5.8783 | 23.0050 | 688 | 87 | 12.0 | 5.5 | 8.4 | 10.27 | 12.28 | 2.57 | 1.20 |
| M50-12 | 5.8795 | 23.0092 | 689 | 85 | 15.6 | 7.0 | 10.6 | 10.35 | 12.47 | 2.44 | 1.20 |

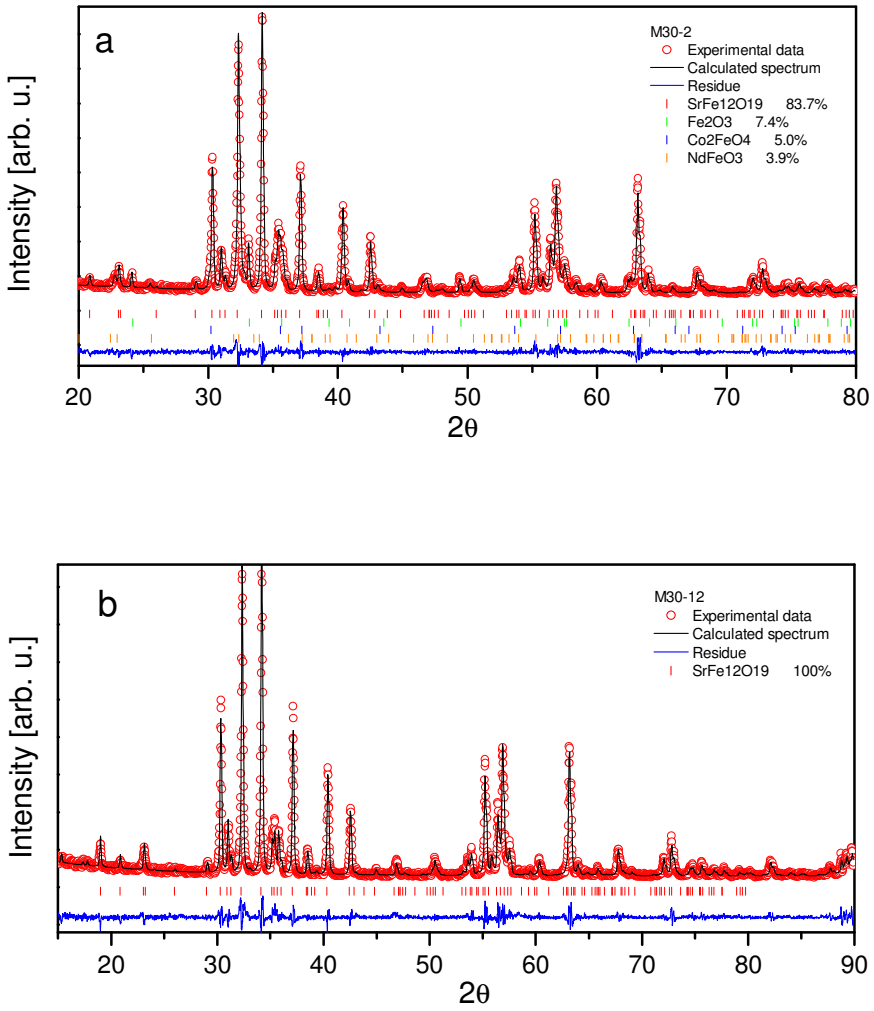


Fig. 2. Observed (red circles ○) and calculated (black continuous line) intensity profiles for M30-2 (a) and M30-12 (b). The short vertical lines indicate the angular position of the allowed Bragg reflections for each phase. At the bottom, the difference plot ($I_{obs}$ - $I_{calc}$) is shown. The structural and refinement parameters for all the samples are given in Table 2.

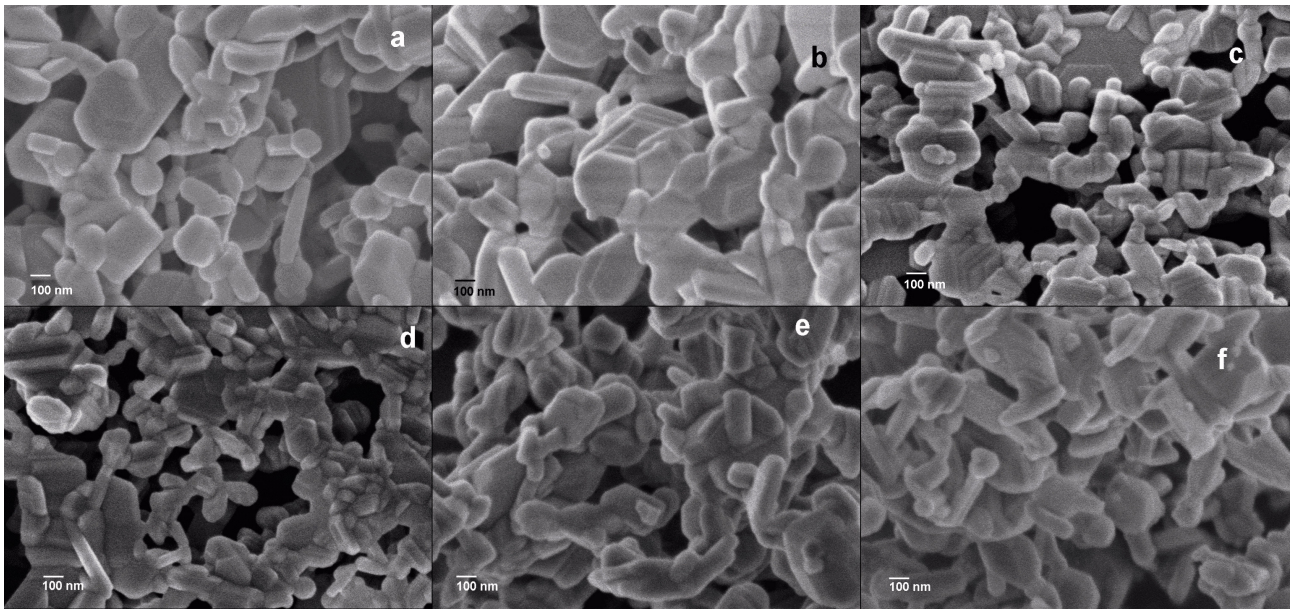


Fig. 3. SEM images of the samples calcined for 2 hours: (a) M0-2, (b) M10-2, (c) M20-2, (d) M30-2, (e) M40-2, (f) M50-2. Bar = 100 nm.

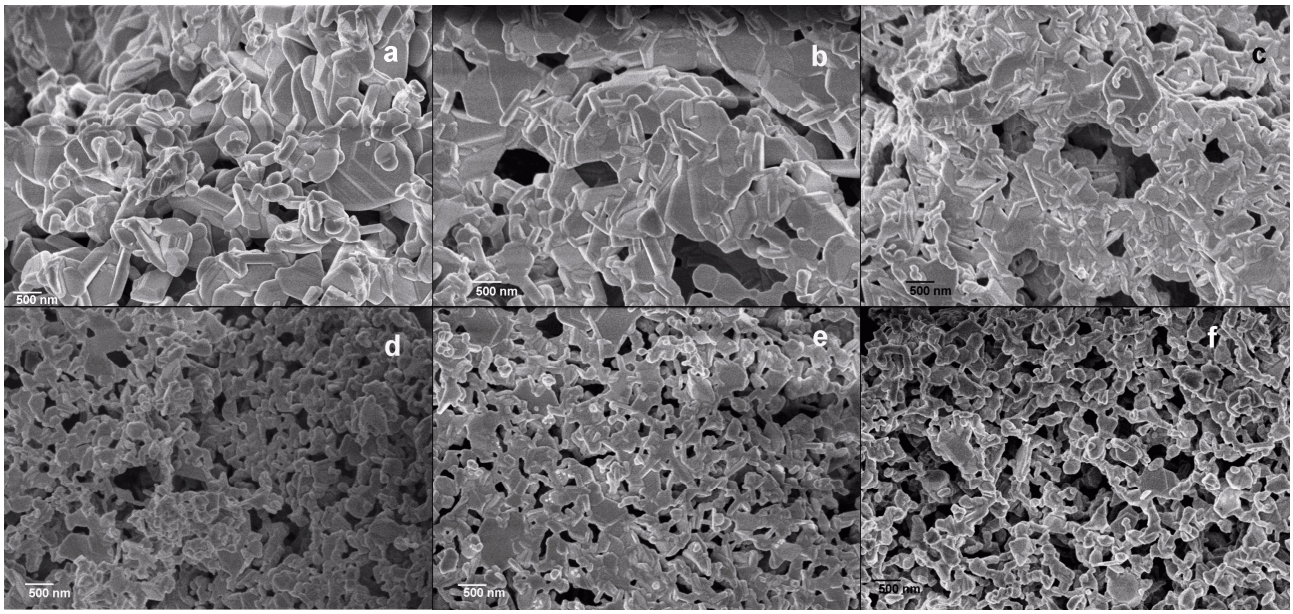


Fig. 4. SEM images of the samples calcined for 12 hours: (a) M0-12, (b) M10-12, (c) M20-12, (d) M30-12, (e) M40-12, (f) M50-12. Bar = 500 nm.

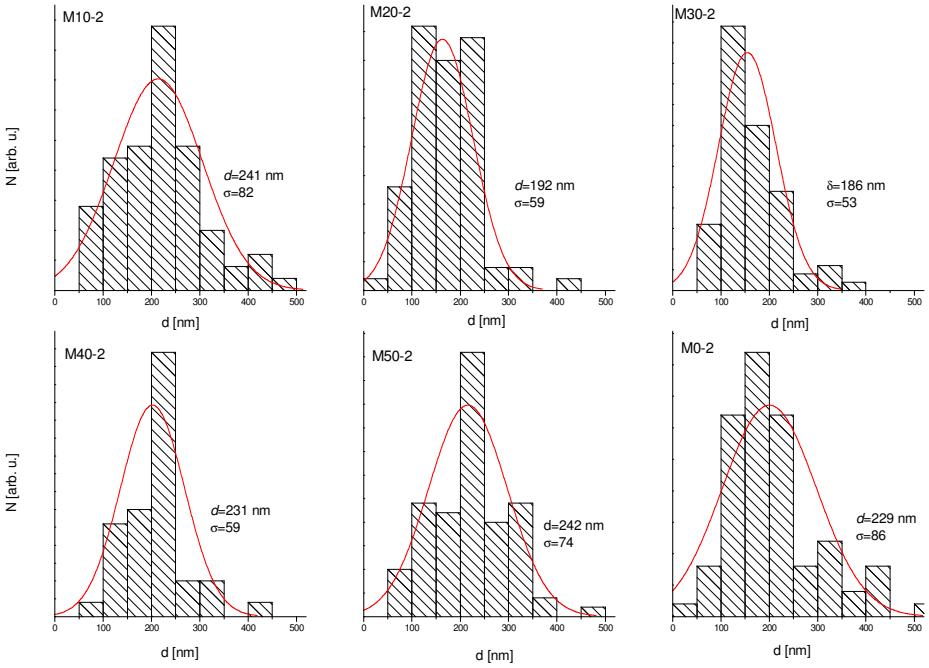


Fig. 5. Histograms for the particle size (*d*) distribution of the set of samples My-2.

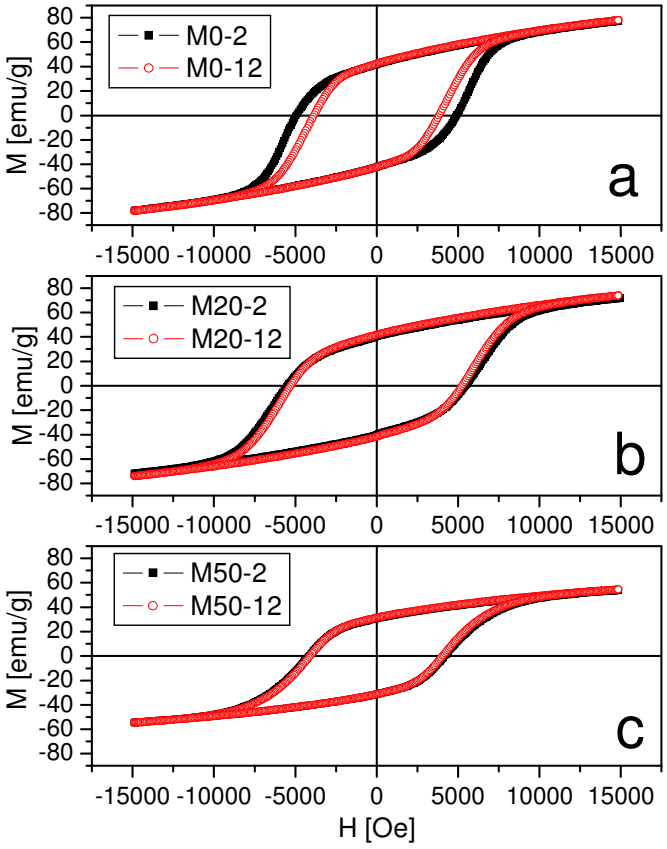


Fig. 6. Hysteresis loops *M vs H* of samples: (a) M0-2 and M0-12, (b) M20-2 and M20-12, and (c) M50-2 and M50-12.

Using ICP results allows for the determination of the cationic composition which is shown in Table 1. These results are close to the nominal composition. Notwithstanding atomic composition for Fe and Co are slightly lower than the expected values. This can be related to some difficulties in these cations' dissolution even when a standard reagent (nitric and perchloric acid) was used.

Figure 6 shows the hysteresis loops of selected samples calcined for 2 and 12 h and Fig. 7 summarizes coercivity $H_C$ and saturation magnetization $M_S$ values for all the studied samples.

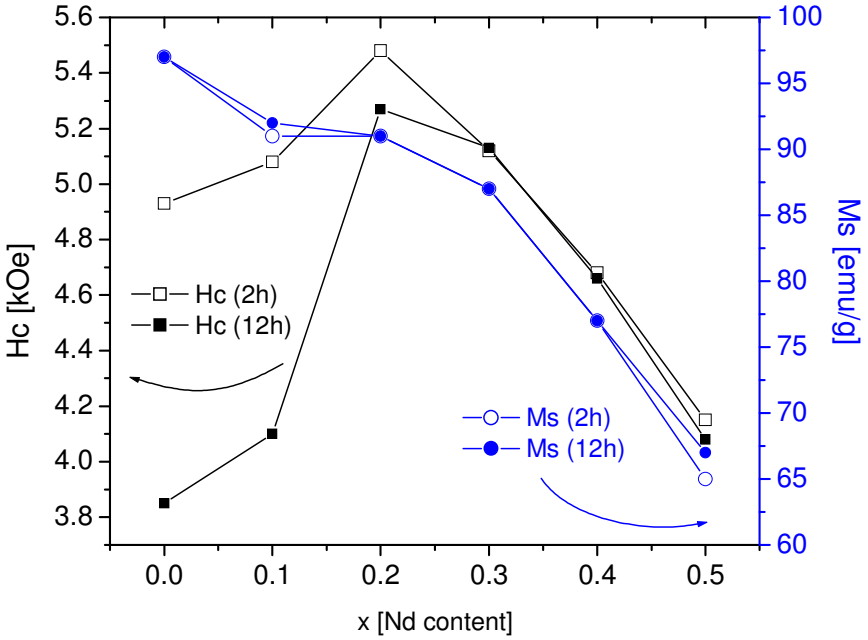


Fig. 7. Saturation magnetization $M_S$ and coercivity $H_C$ as a function of Nd content $x$ for samples calcined for 2 and 12 hours.

In samples calcined for 2 h, coercivity increases with Nd-Co substitution up to $x$=0.2. It has been reported that R-Co substitution modifies the magnetocrystalline anisotropy [9,10]. In the mentioned samples this effect may be the main contribution to the increase in coercivity. For $x \geq 0.3$ the segregated phases ($NdFeO_3$ and $Co_2FeO_4$) and hematite (>7%) cause structural and chemical composition modifications which are responsible for the coercivity decrease.

In samples calcined for 12 h, the same behavior is observed. Notwithstanding, lower values of $H_C$ are measured for samples with x<0.3. This is attributed to the increase in grain size observed in the micrographs of Fig. 4. The rest of the samples do not have a significant variation in $H_C$.

Coercivity increases from 4930 Oe (62.0 A/m) for $x$=0 to 5480 Oe (68.9 A/m) for $x$=0.2 (11 %). It is remarkable that the coercivity of samples My-2 increases with respect to stoichiometric substituted samples and samples with a strong iron deficiency [15]. For $x$=0.3: $H_C$(M30-2)=5130 Oe (64.5 A/m); $H_C(SrNd_{0.3}Fe_{11.7}Co_{0.3}O_{19})$ =4613 Oe (58.0 A/m) and $H_C(SrNd_{0.3}Fe_{8.4}Co_{0.3}O_{19})$ =4670 Oe (58.7 A/m). These results show that the Fe/Sr ratio of the samples presented in this work enhances coercivity for $x$<0.4.

Saturation magnetization $M_S$ is practically the same for samples with the same substitution when calcined for 2 or for 12 h. $M_S$ is slightly reduced with Nd-Co substitution from 97 $Am^2/kg$ (97 emu/g) for $x$=0 to 91 $Am^2/kg$ (91 emu/g) for $x$=0.2. For $x \geq 0.3$ the segregated phases are the responsible for the decrease in $M_S$.

Longer heat treatments increase $M_S$ only slightly and diminish $H_C$, especially in the samples with lower substitution. These results suggest that a longer heat treatment is not justified for obtaining good magnetic properties; therefore, we will continue this work focusing only on the set of samples calcined for 2 h.

Magnetic susceptibility $\chi = dM/dH$ is often computed to evaluate the magnetic interaction in different systems, since this magnitude is related to the inversion-field distribution. The maximum in $dM/dH$ (denoted $\chi H_C$) coincides with coercivity $H_C$ in systems with a single magnetic phase and an unimodal inversion-field distribution.

The susceptibility $\chi$ was calculated as the derivative of $M$ with respect to $H$ of the upper branch of the hysteresis loop and is shown in Figure 8 for samples My-2. The fitting of these curves was performed using the program PeakFit 4.12. The position of the peaks was determined with an error of about ±20 Oe (0.25 A/m) since displacements of this order of magnitude did not alter appreciably the regression coefficient (probably because of the experimental values dispersion). In every case, two magnetic contributions are needed to fit $\chi$ *vs* $H$. In order to understand where these two contributions come from, a detailed analysis on the phases present in each sample is needed.

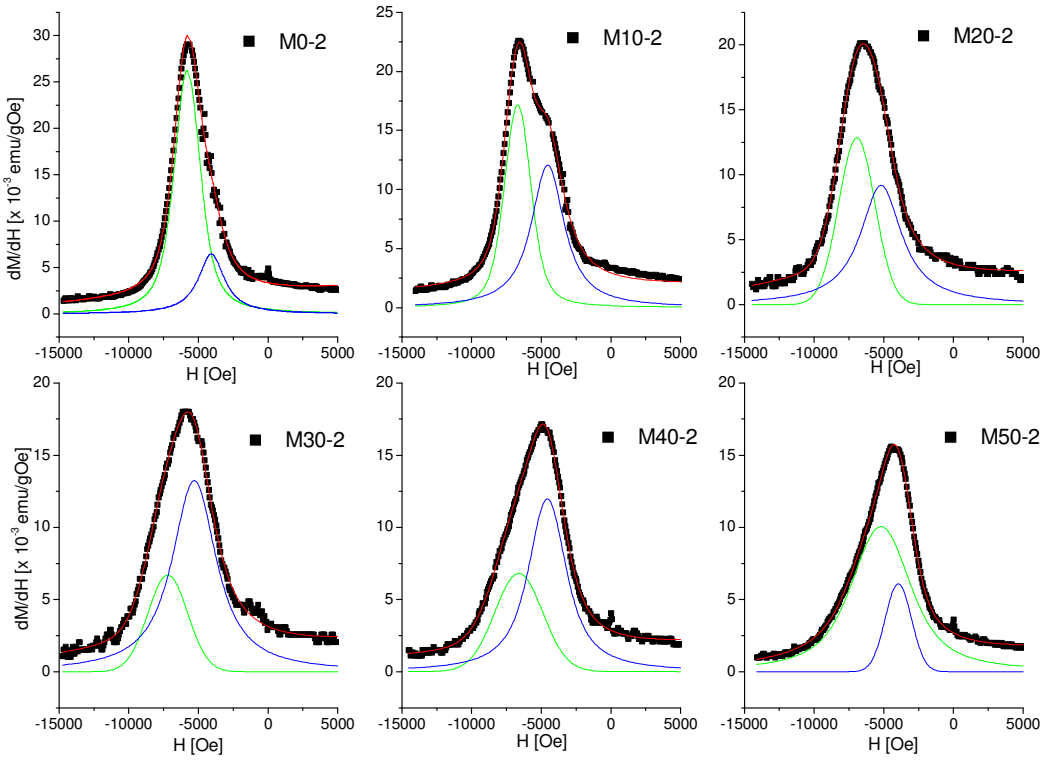


Fig. 8. Magnetic susceptibility $\chi$ as a function of applied field $H$, for samples My-2. The squares are experimental data and the solid lines correspond to the fittings of two Voigt functions (color on line).

$Co_2FeO_4$ is a ferromagnetic spinel. The magnetic properties of this phase are very much sensitive to the preparation techniques. Paneer Muthuselvam *et al.* [18] report $\chi H_C$ values for a set of differently prepared samples which range from 130 to 700 Oe (1.6 to 8.8 A/m) at room temperature. Manova *et al.* [19] inform they obtain a superparamagnetic behavior for $Co_2FeO_4$ nanoparticles of the order of 10 nm.

Nd ferrate or Nd orthoferrite, $NdFeO_3$, is an orthorhombically distorted perovskite which has a very weak ferromagnetic component at room temperature. According to Xu *et al.* [20], nanometric particles of this phase have $M_S$<0.5 emu/g and $H_C$ ~0 Oe.

Hematite –at room temperature– is antiferromagnetic with a weak ferromagnetic component, saturation magnetization of ~0.8 emu/g and coercivities of 100-200 Oe (1.2-2.5 A/m) due to magnetocrystalline anisotropy [21]. Even when hematite with high coercivity has been reported in crystals with defects and internal stresses [21,22], it is not expected that in samples prepared by the self-combustion method and posterior calcination hematite will have a structure with defects or stresses. Even if this were the case, the magnitude of this contribution to d$M$/d$H$ would be at least one order of magnitude smaller than any of the peaks observed in Figure 8.

Samples M0-2 and M10-2 are single phase so the hexaferrite is the only phase responsible for the two contributions to χ. The rest of the samples contain other phases which might have a share in one of the observed peaks. However, from the previous description of the secondary phases found in samples My-2, none of them is likely to contribute appreciably to d$M$/d$H$. A bimodal distribution in particle size could originate the observed behavior in χ. However, this possibility is discarded on the basis of SEM data (see Figure 5). Therefore, the two magnetic contributions observed in χ are assigned to an inhomogeneous cationic distribution and/or a lattice distortion related to the increase in magnetocrystalline anisotropy. These contributions give rise to two magnetic orderings: one with lower $\chi H_C$ ($\chi H_C$1 in Table 3) and another with higher anisotropy regions and therefore higher $\chi H_C$ ($\chi H_C$2 in Table 3). Because of the interaction between these magnetic arrangements, $H_C$ results in an intermediate value of coercivity ($H_C$ in Table 3).

This effect has already been reported on similar samples in a previous paper [23], where the two observed contributions to χ converged into one after sintering, indicating that the harder magnetic phase was originated in an inhomogeneous cationic distribution. In the present case, however, longer calcination times do not anneal out this effect, probably because of the higher occupancy of the crystalline sites due to the higher Fe/Sr ratio selected for this work, which might slow down cation thermal migration.

The Curie temperature $T_C$ of the samples was determined with the aid of TG measurements under an applied magnetic field.

The inset of Figure 9 shows the weight *vs* temperature curve obtained for M0-2. All the samples have similar behaviors, showing two ferro- to paramagnetic transitions, as two steps in the TG curves.

Table 3. Coercivity $H_C$, maxima in d$M$/d$H$ $\chi H_C$1 and $\chi H_C$2, and Curie temperatures $T_C$1 and $T_C$2.

| $x$ | $H_C$ [Oe] | $\chi H_C$1 [emu / g Oe] | $\chi H_C$2 [emu / g Oe] | $T_C$1 [ºC] | $T_C$2 [ºC] |
|---|---|---|---|---|---|
| 0.00 | 4930 | 5800 | 4070 | 454 | 461 |
| 0.10 | 5080 | 6676 | 4494 | 444 | 455 |
| 0.20 | 5480 | 6926 | 5257 | 443 | 454 |
| 0.30 | 5120 | 7187 | 5303 | 440 | 453 |
| 0.40 | 4680 | 6618 | 4567 | 437 | 451 |
| 0.50 | 4150 | 5208 | 3960 | 436 | 450 |

Figure 9 shows the measured values of $T_C$ as a function of Nd-Co content. The observation of two Curie temperatures at $T_C$1 and $T_C$2 ($>T_C$1) provides additional support of the presence of two magnetic arrangements, one corresponding to a moderate ordered structure and another to a more

anisotropic one. The values of $T_C1$ and $T_C2$ for all the samples are indicated in Table 3. In order to correlate each $T_C$ to one of the inversion field distributions observed in $\chi$, the Curie temperature of a stoichiometric sample $SrFe_{12}O_{19}$ prepared by the same method and previously studied [16] was measured. In this case, a single value for $T_C$ was obtained and is shown in Figure 9 with a star. This result suggests that it is possible to relate $T_C1$ to the more ordered magnetic structure. It is remarkable that the existence of two transition temperatures is not related to the substitution, but to the iron deficiency in the formulation, since M0-2 shows this behavior (Table 3) while the stoichiometric sample does not.

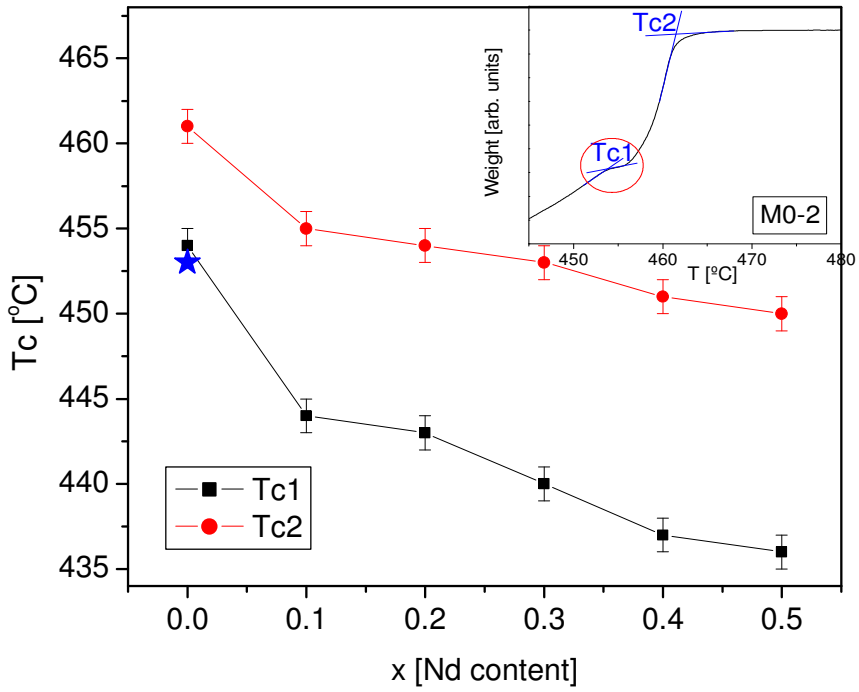


Fig. 9. $T_C1$ and $T_C2$ as a function of Nd content $x$. The star corresponds to the Curie temperature of a stoichiometric sample $SrFe_{12}O_{19}$. Inset: Weight as a function of temperature under an applied magnetic field for sample M0-2.

It is also observed that both $T_C1$ and $T_C2$ decrease with substitution (Figure 9), either because the exchange interaction between Fe ions is reduced as Nd-Co enter the lattice and/or because crystalline disorder increases with substitution.

## 4. Conclusions

Nd-Co substituted hexaferrites $Sr_{1-x}Nd_xFe_{11-x}Co_xO_{19}$ ($x$=0 to 0.5) were successfully prepared by the self-propagating combustion method. M-type hexaferrites are obtained after calcining in air at 1100ºC for two hours.

The magnetic properties of the prepared samples could be enhanced by partial Nd-Co inclusion. Substitution up to $x$=0.3 can be utilized for enhancement of the coercive field ($H_C$) with a slight reduction (6%) in saturation magnetization. Coercivity increases from 4930 Oe (62.0 A/m) for $x$=0 to 5480 Oe (68.9 A/m) for $x$=0.2 (11 %). The coercivities of samples My-2 increase with respect to stoichiometric substituted samples and samples with a strong iron deficiency.

A particular behavior of magnetic susceptibility with applied field is here analyzed. The results are related to inhomogeneous magnetic orderings which translate in two values of $T_C$, suggesting different magnetic interactions.

**Acknowledgements**
The authors are indebted to Joaquín Carpenco for experimental work and Dr. Luis D. Martínez from INQUISAL, Universidad de San Luis for ICP measurements. P. G. Bercoff is particularly indebted to Denise Toomey from Penn Yan, NY, who kindly agreed to check the manuscript for language mistakes. This work was financially supported by Universidad de Buenos Aires (UBACyT, grant I-011), Secyt-UNC and Conicet.

**References**

[1] H. Kojima, in: E.P. Wohlfarth (Editor), *Handbook of Ferromagnetic Materials*, vol. 3, North-Holland, Amsterdam (1982) 305-391.
[2] X. Liu, W. Zhong, S. Yang, Z. Yu, B. Gu, Y. Du, J. Magn. Magn. Mater. 238 (2002) 207-214.
[3] J.M. Le Breton, L. Lechevallier, J.F. Wang, R. Harris, J. Magn. Magn. Mater. 272-276 (2004) 2214-2215.
[4] Y.P. Fu, C.H. Lin, J. Alloys Compd. 386 (2005) 222-227.
[5] S.E. Jacobo, C. Domingo-Pascual, R. Rodríguez-Clemente, M.A. Blesa, J. Mater. Sci. 32 (4) (1997) 1025-1028.
[6] P.G. Bercoff, H.R. Bertorello, J. Magn. Magn. Mater. 205 (1999) 261-269.
[7] J.F. Wang, C.B. Ponton, I.R. Harris, J. Magn. Magn. Mater. 234 (2001) 233-240.
[8] J.F. Wang, C.B. Ponton, I.R. Harris, IEEE Trans. Magn. 38 (5) (2002) 2928-2930.
[9] H. Taguchi, Y. Minachi, K. Masuzawa, H. Nishio, in: *Proceedings of the Eighth International Conference on Ferrites* (2000) p. 405.
[10] F. Kools, A. Morel, R. Grössinger, J.M. Le Breton, P. Tenaud, J. Magn. Magn. Mater. 242-245 (2002) 1270-1276.
[11] P. Tenaud, A. Morel, F. Kools, J.M. Le Breton, L. Lechevallier, J. Alloys Compd. 370 (2004) 331-334.
[12] M.I. Oliva, P.G. Bercoff, H.R. Bertorello, J. Magn. Magn. Mater. 320 (14) (2008) e100-e103.
[13] L. Lechevallier, J.M. Le Breton, A. Morel, P. Tenaud, J. Magn. Magn. Mater. 316 (2007) e109-e111.
[14] Q.Q. Fang, H.W. Bao, D.M. Fang, J.Z. Wang, X.G. Li, J. Magn. Magn. Mater. 278 (2004) 122-126.
[15] P.G. Bercoff, C. Herme, S.E. Jacobo, J. Magn. Magn. Mater. 321 (2009) 2245-2250.
[16] C. Herme, S.E. Jacobo, P.G. Bercoff, B. Arcondo, Hyperfine Inter. 195 (1-3) (2010) 205-212.
[17] N. Rezlescu, C. Doroftei, E. Rezlescu, P.D. Popa, J. Alloys Compd. 451 (2008) 492-496.
[18] I. Panneer Muthuselvam, R.N. Bhowmik, Solid State Sciences 11 (3) (2009) 719-725.
[19] E. Manova, D. Paneva, B. Kunev, Cl. Estournès, E. Rivière, K. Tenchev, A. Léaustic, I. Mitov, J. Alloys Compd. 485 (2009) 356-361.
[20] H. Xu, X. Hu, L. Zhang, Crystal Growth & Design 8 (7) (2008) 2061-2065.
[21] D.J. Dunlop, Ö. Özdemir, *Rock Magnetism: Fundamentals and Frontiers*, Cambridge studies in magnetism, Cambridge University Press (2001) chapter 3.
[22] P.G. Bercoff, H.R. Bertorello, Applied Physics A 100 (4) (2010) 1019-1027.
[23] S.E. Jacobo, C. Herme, P.G. Bercoff, J. Alloys Compd. 495 (2) (2010) 513-515.
[24] R. Grössinger, C. Tellez Blanco, M. Küpferling, M. Müller, G. Wiesinger, Physica B 327 (2003) 202-207.